J. Comput. Phys. **226** (2007) 2229–2249, doi:10.1016/j.jcp.2007.07.007

An Arbitrary Lagrangian-Eulerian method for simulating bubble growth in polymer foaming

Pengtao Yue[1], James J. Feng[1]*, Christopher A. Bertelo[2], and Howard H. Hu[3]

[1]Department of Chemical and Biological Engineering and Department of Mathematics
University of British Columbia, Vancouver, BC V6T 1Z3, Canada

[2]Arkema Research Center, 900 First Avenue, King of Prussia, PA 19406, USA

[3]Department of Mechanical Engineering and Applied Mechanics
University of Pennsylvania, Philadelphia, PA 19104, USA

Abstract - We present a sharp-interface algorithm for simulating the diffusion-driven bubble growth in polymer foaming. A moving mesh of unstructured triangular elements tracks the expanding and deforming bubble surface. In the interior of the liquid, the mesh velocity is determined by solving a Laplace equation to ensure spatially smooth mesh movement. When mesh distortion becomes severe, remeshing and interpolation are performed. The governing equations are solved using a Galerkin finite-element formalism, with fully implicit time marching that requires iteration among the bubble and mesh deformation, gas diffusion and the flow and stress fields. Besides numerical stability, the implicit scheme also guarantees a smooth interfacial curvature as numerical disturbances on the interface are automatically relaxed through the iterations. The polymer melt is modeled as a viscoelastic Oldroyd-B fluid. First, we compute three benchmark problems to validate various aspects of the algorithm. Then we use a periodic hexagonal cell to simulate bubble growth in an isothermal two-dimensional foam, fed by a gaseous blowing agent initially dissolved in the melt to supersaturation. Results show two distinct stages: a rapid initial expansion followed by slow drainage of the liquid film between bubbles driven by capillarity. The effect

---

*Corresponding author. E-mail jfeng@CHML.UBC.CA

of viscoelastic rheology is to enhance the speed of bubble growth in the first stage, and hinder film drainage in the second. Finally, we use axisymmetric simulations to investigate the thinning film between a bubble and a free surface. Melt viscoelasticity is shown to initially enhance film thinning but later resist it. An important insight from the simulations is that polymer strain-hardening, namely the steep increase of elongational viscosity with strain, helps stabilize the foam structure by suppressing bubble-bubble coalescence and bubble burst at the foam surface. This confirms prior observations in foam extrusion experiments.

Keywords: Free surface problem; Interfacial flows; Moving mesh; Finite elements; Viscoelasticity; Oldroyd-B fluids; Film drainage; Capillarity

1 Introduction

Foams are an important class of industrial materials with diverse applications such as in packaging, insulation, personal care and fire retardation [1]. Although a wide range of materials can be foamed, including carbon, ceramics and metals [2–4], aqueous foams and polymer foams are the most common. Aqueous foams have received much attention as a prototypical soft matter, and a more or less coherent understanding has taken shape on their structure, deformation and microrheology [5–7]. Polymer foams, on the other hand, are used in the solid state. Their properties depend critically on the foaming process, from nucleation of microbubbles to their subsequent growth driven by gas diffusion. Fluid dynamics and rheology play central roles in this process. Despite much effort, our theoretical understanding of polymer foaming remains relatively primitive, at least in comparison with that in aqueous foams.

Modeling and numerical simulation of polymer foaming are difficult tasks. First, microbubbles nucleate mostly heterogeneously on defects, impurities or nucleating agents in the polymer melt [8]. A widely applicable and satisfactory nucleation model is not yet available. Consequently, most theoretical work has concentrated on bubble growth from prescribed initial conditions. Second, real foams have a more or less random structure, with bubbles growing next to neighbors of various sizes and proximity. This is typically circumvented by using one-dimensional (1D) models of a single spherical bubble growing within a spherical shell [9]. Recently, 2D periodic cells have been used to represent bubble-bubble interactions [10,11]. Third, the growing and deforming bubbles represent a moving-boundary problem. Several numerical methods have been developed for interfacial flows, such as the volume-of-fluid (VoF) [12,13], level set [14], front tracking [15,16], moving mesh [17], lattice Boltzmann [18,19] and phase-field methods [20]. However, the foaming process has several special features. The flow in the melt is coupled with gas diffusion that drives the bubble expansion. The non-Newtonian rheology of the polymer melt must be incorporated into the flow equations. One may neglect the gas flow within the bubble and treat the bubble surfaces as free boundaries. But the gas compressibility must be accounted for by an equation of state. Finally, the polymer properties are often modified by plasticization and temperature variations [21].

Numerous 1D models have been developed, which have incorporated non-Newtonian rheology [8, 22–24], temperature effects [25] and plasticization [26]. In comparison, 2D computations are scarce. Popinet and Zaleski [27] used front tracking to calculate the cavitation problem where the bubble pressure is given by a polytropic law for adiabatic compression. Caboussat *et al.* [28, 29] used a VoF technique to calculate the free surface flow of compressible gas bubbles surrounded by incompressible liquids. Beechem *et al.* [3] used front tracking to calculate single bubble growth in Newtonian carbon foams in a rectangular domain. So far, the most detailed numerical simulation on polymer foaming is due to Everitt *et al.* [10, 11], who used a split Eulerian-Lagrangian finite element method to compute bubble growth in a 2D periodic foam. The polymer viscoelasticity is shown to produce a thicker and more uniform film by drawing fluid back from Plateau borders.

The numerical method described in this paper is based on the same idea of reconciling Eulerian and Lagrangian descriptions in moving-boundary problems. This is achieved by an arbitrary Lagrangian-Eulerian (ALE) scheme using a mesh velocity [30]. The governing equations are solved by finite elements on a moving grid, with fully implicit updating of the bubble surface. After describing the algorithm, we present three benchmark calculations that validate various aspects of the method and the code. Then we simulate the diffusion-driven growth of bubbles in polymer foaming in a 2D periodic cell. Our results confirm those of Everitt *et al.* [10] on the viscoelastic effects. Furthermore, we explore an intriguing non-monotonic dependence of bubble growth on the Deborah number, which reveals the central role of melt strain-hardening in polymer foaming. Finally, we investigate the film drainage between a bubble and a free surface as is relevant to bubble burst frequently seen in foaming operations.

2 Mathematical formulation and numerical algorithm

2.1 Governing equations

A gas bubble in a polymer melt is illustrated in Fig. 1. Its expansion involves three processes: flow of the polymer melt, gas diffusion in the polymer melt, and isothermal expanding of the gas bubble.

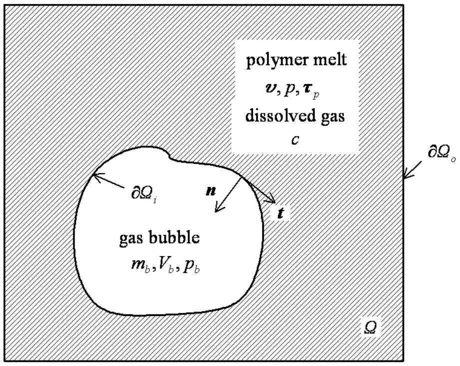

Figure 1: Schematic of a gas bubble in a polymer melt. Ω is the computational domain with inner boundary $\partial\Omega_i$ and outer boundary $\partial\Omega_o$. Pressure p, velocity $\boldsymbol{v}$, polymer stress $\boldsymbol{\tau}_p$ and gas concentration c are to be solved in the polymer melt, while the bubble mass m_b, volume V_b and pressure p_b need to be calculated for the bubble.

For the polymer melt, the governing equations include the momentum equation

$$\rho\left(\frac{\partial \boldsymbol{v}}{\partial t} + \boldsymbol{v}\cdot\nabla\boldsymbol{v}\right) = -\nabla p + \nabla\cdot\boldsymbol{\tau} + \rho\boldsymbol{g} \tag{1}$$

and the continuity equation

$$\nabla\cdot\boldsymbol{v} = 0, \tag{2}$$

where ρ, $\boldsymbol{v}$, t, p, $\boldsymbol{\tau}$ and $\boldsymbol{g}$ are melt density, velocity, time, pressure, stress and body force, respectively. The viscoelastic rheology is represented by the Oldroyd-B model, which, to be strict, is for dilute polymer solutions [31]. However, this simple model is easy to implement numerically and does capture the essential rheological features of interest here, such as strain-hardening. Thus, the stress in the melt is expressed as the sum of a viscous "solvent" stress and a polymer stress: $\boldsymbol{\tau} = \boldsymbol{\tau}_s + \boldsymbol{\tau}_p = \mu_s[\nabla\boldsymbol{v} + (\nabla\boldsymbol{v})^T] + \boldsymbol{\tau}_p$, μ_s being a "solvent" viscosity. $\boldsymbol{\tau}_p$ is given by the following constitutive equation:

$$\boldsymbol{\tau}_p + \lambda_H\left[\frac{\partial\boldsymbol{\tau}_p}{\partial t} + \boldsymbol{v}\cdot\nabla\boldsymbol{\tau}_p - \boldsymbol{\tau}_p\cdot(\nabla\boldsymbol{v}) - (\nabla\boldsymbol{v})^T\cdot\boldsymbol{\tau}_p\right] = \mu_p[\nabla\boldsymbol{v} + (\nabla\boldsymbol{v})^T], \tag{3}$$

where λ_H, μ_p are relaxation time and viscosity of the polymer. The total viscosity of polymer melt is given by $\mu = \mu_s + \mu_p$.

Gas diffusion in the polymer melt is governed by a convection-diffusion equation

$$\frac{\partial c}{\partial t} + \boldsymbol{v}\cdot\nabla c = \nabla\cdot(D\nabla c), \tag{4}$$

where c and D are the gas concentration and diffusivity in the polymer melt. Although c is typically the mass fraction of gas in the polymer, it is dimensionally more convenient here to define it as the gas density, namely the gas mass per unit volume of the melt.

Each bubble gains mass at a rate equal to the mass flux of dissolved gas (blowing agent) diffusing into the bubble:

$$\frac{dm_b}{dt} = -\oint_{\partial\Omega_i} D\nabla c \cdot \boldsymbol{n} dS, \tag{5}$$

where m_b is the gas mass inside the bubble, $\boldsymbol{n}$ is the normal direction to the bubble surface $\partial\Omega_i$ pointing into the bubble. The gas in the bubble remains at thermodynamic and mechanical equilibrium, and obeys the ideal gas law:

$$p_b V_b = m_b R T, \tag{6}$$

where p_b is the gas pressure, V_b is the bubble volume, and R and T are the specific gas constant and absolute temperature. In this paper, we only consider the isothermal case where T is a constant.

Equations (1–6) form the governing equations for polymer foaming. Among these, Eq. (5) is an ordinary differential equation and Eq. (6) is a simple algebraic equation. Only Eqs. (1–4) need to be solved on a spatial grid.

2.2 Boundary conditions

On the inner boundary $\partial\Omega_i$, i.e., the bubble surface, we assume there is no surfactant and thus the shear stress is zero. The normal stress obeys the Young-Laplace equation:

$$\boldsymbol{n} \cdot (-p\boldsymbol{I} + \boldsymbol{\tau}) = (-p_b + K\sigma)\,\boldsymbol{n}, \tag{7}$$

where σ is the surface tension, $\boldsymbol{n}$ is the normal to bubble surface (see Fig. 1), and K is the surface curvature in 2D or twice the mean curvature in 3D. Gas concentration is given by Henry's law:

$$c = k p_b, \tag{8}$$

where k is the Henry's law constant.

On the outer boundary $\partial\Omega_o$, we can either impose a fixed far-field gas concentration ($c = c_\infty$) or a zero flux condition ($\frac{\partial c}{\partial \boldsymbol{n}} = 0$) depending on the physical setup of the problem. For the flow field, various portions of $\partial\Omega_o$ may have no-slip, slip, prescribed stress or "moving wall" conditions. These will be described in Section 3 for specific problems.

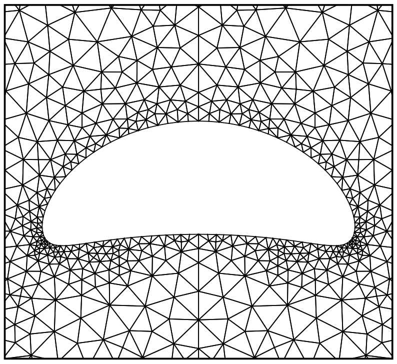

Figure 2: Triangular mesh around a non-spherical bubble, with refined elements at the bubble tips where the surface curvature is high.

2.3 Mesh adaptation and moving mesh scheme

The governing equations are solved in 2D planar and axisymmetric geometries on a triangular mesh, which moves and deforms according to an arbitrary Lagrangian-Eulerian (ALE) scheme [30,32]. Curved P_2 triangles (six nodes) are used to better fit the curved boundaries. Mesh adaptation is achieved by the addition, removal and redistribution of boundary nodes.

Initially, the outer boundary $\partial\Omega_o$ is divided into segments of size h_0 and the inner boundary $\partial\Omega_i$ of a typically much smaller size h_1. Then the bulk mesh is generated by Delaunay triangulation [33,34]. During this process, smoothing is used to ensure a gradual variation of the mesh size throughout the domain. During the simulation, boundary deformation may necessitate mesh refinement on $\partial\Omega_i$ and even $\partial\Omega_o$. This is determined according to two criteria: surface curvature and proximity between two boundaries. On $\partial\Omega_i$, the boundary mesh is refined at larger curvature and coarsened at lower curvature, within the range of $[0.1h_1, 2h_1]$, so each boundary segment subtends roughly the same central angle. Figure 2 shows an example of such refinement. Note that the minimum resolvable length is $0.1h_1$ and smaller surface features will be smoothed out. When two surfaces approach each other, the thin film between them is resolved by reducing the mesh size on the surfaces to a fraction, usually 1/3, of the film thickness. An example can be found in Fig. 16(b).

At every time step, the mesh quality is checked by comparing the volume and aspect ratio of each element with their initial values in the undeformed mesh [30]. Distortions arise from the relative motion of internal surfaces as well as the refinement or coarsening of the surface nodes described above. If mesh distortion exceeds a threshold, the whole computational domain is remeshed, and the field variables are mapped from the old mesh to new mesh by a global least-squares projection scheme [30].

ALE centers on the simultaneous use of two coordinate systems: an Eulerian coordinate $\boldsymbol{x}$ and a quasi-Lagrangian coordinate $\boldsymbol{X}$ affixed to the moving mesh. Thus the mesh velocity is given by:

$$\boldsymbol{v}_m(\boldsymbol{x}, t) = \frac{\partial \boldsymbol{x}(\boldsymbol{X}, t)}{\partial t}. \tag{9}$$

On the domain boundary (including the bubble surface) the mesh velocity conforms to that of the boundary with possible slip. Inside the domain, mesh velocity is given by the following Laplace equation:

$$\nabla \cdot (k^e \nabla \boldsymbol{v}_m) = 0, \tag{10}$$

where k^e is the inverse of the local element volume [30,32]. In the moving mesh system, the variables are defined based on $\boldsymbol{X}$ instead of $\boldsymbol{x}$, thus the material derivatives in the governing equations will be replaced by the referential time derivatives $\frac{\delta}{\delta t} = \frac{\partial}{\partial t}\big|_{\text{fix } \boldsymbol{X}}$:

$$\frac{d}{dt} = \frac{\partial}{\partial t} + \boldsymbol{v} \cdot \nabla = \frac{\delta}{\delta t} + (\boldsymbol{v} - \boldsymbol{v}_m) \cdot \nabla. \tag{11}$$

If $\boldsymbol{v}_m = \boldsymbol{v}$, the mesh would follow the local fluid flow and thus be fully Lagrangian. Note that the mesh velocity and other time-dependent governing equations are coupled. After we obtain the mesh velocity at a new time, the mesh position can be updated by integrating Eq. (9).

2.4 Finite-element formulation

The discretization of the governing equations follows the standard Galerkin formalism. We seek the following weak solutions: $(\boldsymbol{v}, p, \boldsymbol{\tau}_p) \in \mathcal{U} \times \mathcal{P} \times \mathcal{T}$, $c \in \mathcal{C}$ and $\boldsymbol{v}_m \in \mathcal{U}_m$. For 2D flows, the solution spaces satisfy $\mathcal{U} \in H^1(\Omega)^2$, $\mathcal{P} \in L^2(\Omega)$, $\mathcal{T} \in L^2(\Omega)^3$ ($L^2(\Omega)^4$ for axisymmetric flow), $\mathcal{C} \in H^1(\Omega)$, and $\mathcal{U}_m \in H^1(\Omega)$. Note that the computational domain Ω varies with the moving boundary. Using basis functions $(\tilde{\boldsymbol{v}}, \tilde{p}, \tilde{\boldsymbol{\tau}}) \in \mathcal{U} \times \mathcal{P} \times \mathcal{T}$, we write the following weak forms of the flow equations:

$$\int_\Omega \left\{ \left[\rho \left(\frac{\delta \boldsymbol{v}}{\delta t} + (\boldsymbol{v} - \boldsymbol{v}_m) \cdot \nabla \boldsymbol{v} - \boldsymbol{g} \right) \right] \cdot \tilde{\boldsymbol{v}} + (-p\boldsymbol{I} + \boldsymbol{\tau}) : \nabla \tilde{\boldsymbol{v}} \right\} x^\alpha d\Omega - S = 0, \quad (12)$$

$$\int_\Omega -(\nabla \cdot \boldsymbol{v}) \tilde{p}\, x^\alpha d\Omega = 0, \quad (13)$$

$$\begin{aligned} \int_\Omega \Big\{ \boldsymbol{\tau}_p + \lambda_H \left[\frac{\delta \boldsymbol{\tau}_p}{\delta t} + (\boldsymbol{v} - \boldsymbol{v}_m) \cdot \nabla \boldsymbol{\tau}_p - \boldsymbol{\tau}_p \cdot (\nabla \boldsymbol{v}) - (\nabla \boldsymbol{v})^T \cdot \boldsymbol{\tau}_p \right] \\ -\mu_p \left[\nabla \boldsymbol{v} + (\nabla \boldsymbol{v})^T \right] \Big\} : \tilde{\boldsymbol{\tau}}\, x^\alpha d\Omega = 0, \quad (14) \end{aligned}$$

where $\alpha = 0$ for 2D planar geometry and $\alpha = 1$ for axisymmetric geometry with x being the radial coordinate. In this paper, the double dot product between tensors is defined as $\boldsymbol{a} : \boldsymbol{b} = \sum_{ij} a_{ij} b_{ij}$. S is the surface integral of stress boundary conditions:

$$\begin{aligned} S &= \int_{\partial\Omega} \boldsymbol{n} \cdot (-p\boldsymbol{I} + \boldsymbol{\tau}) \cdot \tilde{\boldsymbol{v}}\, x^\alpha dS \\ &= \int_{\partial\Omega_i} (-p_b + K\sigma) \boldsymbol{n} \cdot \tilde{\boldsymbol{v}}\, x^\alpha dS + \int_{\partial\Omega_\tau} \boldsymbol{n} \cdot (-p\boldsymbol{I} + \boldsymbol{\tau}) \cdot \tilde{\boldsymbol{v}}\, x^\alpha dS, \quad (15) \end{aligned}$$

where $\partial\Omega_\tau$ is part of the outer boundary on which stress or "moving wall" boundary conditions are imposed. An example of the latter is given in Section 3.4.

Similarly, by using $\tilde{c} \in \mathcal{C}$ and $\tilde{\boldsymbol{v}}_m \in \mathcal{U}_m$ we write the weak formulations for gas concentration and mesh velocity as:

$$\int_\Omega \left\{ \left[\frac{\delta c}{\delta t} + (\boldsymbol{v} - \boldsymbol{v}_m) \cdot \nabla c \right] \tilde{c} + D \nabla c \cdot \nabla \tilde{c} \right\} x^\alpha d\Omega = 0, \quad (16)$$

$$\int_\Omega k^e \nabla \boldsymbol{v}_m : \nabla \tilde{\boldsymbol{v}}_m\, d\Omega = 0. \quad (17)$$

The nonlinear system of Eqs. (12–14) is solved by Newton's method. The resulting linear system within each Newton iteration and the linear systems of Eqs. (16) and (17) are solved using iterative methods such as the preconditioned generalized minimum residual (GMRES) scheme or biconjugate gradient stabilized (BICGSTAB) algorithm. The use of preconditioners is critical to numerical convergence and more details and references may be found in Hu *et al.* [30].

2.5 Evaluation of the surface tension force

Equation (15) contains the surface tension force: $S_t = \int_{\partial\Omega_i} K\sigma\boldsymbol{n}\cdot\tilde{\boldsymbol{v}}\, x^\alpha dS$. Given the position of surface nodes, we have used two different schemes to evaluate S_t. One is to calculate the curvature K directly from the parabola [35] or circumcircle going through three consecutive surface nodes. This method is straightforward and easily generalized to 3D surfaces [36]. However, numerical errors imply that the surface force integrated over a closed loop does not necessarily vanish. The second scheme, based on integrating the surface tension along the tangent, explicitly ensures the vanishing of the total surface force on any closed loop or surface [15].

In most cases that we have tested, the two methods give essentially identical results. In viscoelastic flows, the tangential integration method sometimes seems less stable than the other. It has been reported that direct calculation of K is liable to oscillations even when the surface appears smooth. These have been suppressed either by a straightforward filtering of the high frequency modes or by a more sophisticated fairing algorithm [16]. Our method is unaffected by such oscillations because the interface is updated implicitly. During the iterations, surface tension smooths out kinks caused by numerical disturbances.

2.6 Temporal discretization and iteration scheme

The nonlinear systems are solved implicitly to enhance stability. The referential time derivatives $\frac{\delta}{\delta t}$ in Eqs. (12, 14, 16) are approximated by second-order schemes such as the Crank-Nicolson scheme [30]:

$$\left(\frac{\delta \boldsymbol{v}}{\delta t}\right)^{n+1} = 2\frac{\boldsymbol{v}^{n+1} - \boldsymbol{v}^n}{\Delta t^{n+1}} - \left(\frac{\delta \boldsymbol{v}}{\delta t}\right)^n, \tag{18}$$

where the superscript n and $n+1$ stand for time steps, and $\Delta t^{n+1} = t^{n+1} - t^n$. Typically, the time step is adjusted automatically according to a set of criteria, including the mesh quality and the amount of surface movement in each step. Within each time step, the whole system is solved iteratively through the following steps:

1. Check mesh quality. If mesh quality is too low, then remesh the whole computational domain, and project all the field variables at t^n to the new mesh.

2. Prepare for iteration.
   (a) Set the initial guess for the variables at t^{n+1} to their values at t^n: $\boldsymbol{v}^* = \boldsymbol{v}^n$, $\boldsymbol{\tau}_p^* = \boldsymbol{\tau}_p^n$, and so on, where * denotes an estimation for the $(n+1)$th step.
   (b) Move the mesh based on a first-order integration of Eq. (9):
   $$\boldsymbol{x}_m^* = \boldsymbol{x}_m^n + \Delta t^{n+1} \boldsymbol{v}_m^n, \tag{19}$$
   where $\boldsymbol{x}_m$ is the position of mesh nodes. If the mesh quality deteriorates below a prescribed standard, decrease Δt^{n+1} and iterate this step until mesh quality is acceptable.
   (c) Estimate bubble mass according to a first-order scheme
   $$m_b^* = m_b^n + \Delta t^{n+1} \left(\frac{dm_b}{dt} \right)^n. \tag{20}$$

3. Iterate until $\boldsymbol{v}^*$, p^*, $\boldsymbol{\tau}_p^*$, $\boldsymbol{v}_m^*$, c^* and m_b^* converge.
   (a) Based on the mesh $\boldsymbol{x}^*$, calculate the bubble volume V^* and the curvature of bubble surface K^*. Update bubble pressure p_b^* based on the new V^* and m_b^* according to Eq. (6). Use K^* and p_b^* to further update the stress and gas concentration conditions at bubble surface according to Eqs. (7) and (8).
   (b) Solve the flow equations (12, 13, 14) by Newton-Krylov methods to get new estimates $\boldsymbol{v}^*$, p^*, and $\boldsymbol{\tau}_p^*$.
   (c) Solve the convection-diffusion equation (16) for gas concentration c^*.
   (d) Based on c^*, calculate the gas flux into the bubble $\left(\frac{dm_b}{dt}\right)^*$ from Eq. (5), and update the bubble mass:
   $$m_b^* = m_b^n + \frac{\Delta t^{n+1}}{2} \left[\left(\frac{dm_b}{dt} \right)^n + \left(\frac{dm_b}{dt} \right)^* \right]. \tag{21}$$
   (e) Update the boundary condition for mesh velocity according to $\boldsymbol{v}^*$, and solve Eq. (17) for the new mesh velocity $\boldsymbol{v}_m^*$.
   (f) Move the mesh according to a second-order scheme:
   $$\boldsymbol{x}_m^* = \boldsymbol{x}_m^n + \frac{\Delta t^{n+1}}{2} \left(\boldsymbol{v}_m^n + \boldsymbol{v}_m^* \right). \tag{22}$$
   If the mesh equality falls below the prescribed threshold, then decrease Δt^{n+1} and go back to step 2.

4. Upon convergence, set $\boldsymbol{v}^{n+1} = \boldsymbol{v}^*$, $p^{n+1} = p^*$, $\boldsymbol{\tau}_p^{n+1} = \boldsymbol{\tau}_p^*$, $c^{n+1} = c^*$, $m_b^{n+1} = m_b^*$, $\left(\frac{dm_b}{dt}\right)^{n+1} = \left(\frac{dm_b}{dt}\right)^*$, $V_b^{n+1} = V_b^*$, $p_b^{n+1} = p_b^*$, $\boldsymbol{v}_m^{n+1} = \boldsymbol{v}_m^*$ and $\boldsymbol{x}_m^{n+1} = \boldsymbol{x}_m^*$. Move on to the next time step.

Numerical experiments indicate that Eq. (21) is prone to oscillations due to overcorrection. If numerical errors cause the gas flux $\left(\frac{dm_b}{dt}\right)^*$ to be overpredicted, it will result in an overpredicted bubble mass m_b^* and pressure p_b^*. The latter raises the gas concentration at the bubble surface via Henry's law and thus lowers the gas flux into air bubbles. In the next iteration, the overpredicted gas flux will be lowered, but often undershooting the eventually converged value. This numerical oscillation is more prominent at larger Δt and may even lead to divergence. To avoid such oscillations, we introduce a damping mechanism by replacing Eq. (21) by

$$(m_b^*)^{i+1} = m_b^n + \frac{\Delta t^{n+1}}{2}\left[\left(\frac{dm_b}{dt}\right)^n + \tilde{f}\right], \tag{23}$$

where $\tilde{f} = (1-c)f^{i+1} + cf^i$, $f = \left(\frac{dm_b}{dt}\right)^*$, $i+1$ and i denote values in the current and previous iteration. $c \in [0,1)$ is a constant defined as:

$$c = \begin{cases} 0 & \text{when } (\delta f^{i+1}\delta f^i) \geq 0 \\ \frac{|\delta f^{i+1}|}{|\delta f^i| + |\delta f^{i+1}|} & \text{when } (\delta f^{i+1}\delta f^i) < 0 \end{cases}, \tag{24}$$

where $\delta f^{i+1} = f^{i+1} - f^i$ is the variation of gas flux between two subsequent iterations. When there is no oscillation in δf, then $c = 0$ and Eq. (23) reduces to Eq. (21). Once oscillation in f is detected, $\tilde{f}$ is taken to be the weighted average between two iterations. This scheme turns out to be very effective and enables us to take full advantage of the implicity by allowing a large Δt.

3 Numerical results

We will describe simulations of five problems. The first three, oscillation of a spherical bubble, rising of a bubble in a quiescent fluid, and diffusion-driven growth of a single bubble, are intended to validate various aspects of our numerical method and code through comparison with known solutions. The other two, diffusion-driven growth of multiple bubbles and film drainage between a bubble and a free surface, explore new physics relevant to polymer foaming, especially the role of viscoelasticity of the polymer melt.

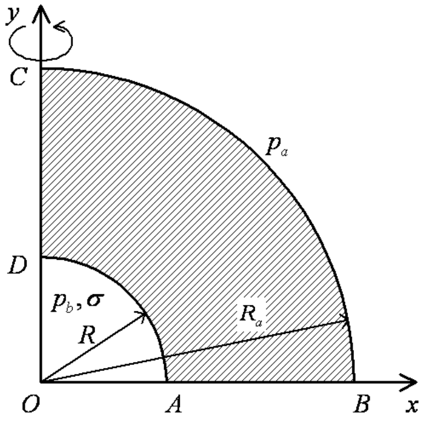

Figure 3: Schematic of a spherical bubble of radius R surrounded by a fluid shell of outer radius R_a.

3.1 Radial oscillation of a spherical bubble

Consider a spherical bubble in an infinite domain of a viscous liquid in which the gas is insoluble. In response to a disturbance in bubble size or pressure, the bubble executes a damped oscillation that is described by the Rayleigh-Plesset equation [37]. This 1D solution has been used by Popinet and Zaleski [27] to validate their numerical code. We compute the oscillation of a bubble surrounded by a fluid shell (Fig. 3), whose outer edge is subject to ambient pressure p_a. The liquid viscosity is μ and its density ρ. The surface tension is σ on the bubble surface. Neglecting the surface tension on the outer edge of the fluid, we write the modified Rayleigh-Plesset equation:

$$R\ddot{R}\left(1-\frac{R}{R_a}\right)+\frac{3}{2}\dot{R}^2\left(1-\frac{4R}{3R_a}\right)=\frac{1}{\rho}\left\{p_b-p_a-\frac{4\mu\dot{R}}{R}\left[1-\left(\frac{R}{R_a}\right)^3\right]-\frac{2\sigma}{R}\right\}, \tag{25}$$

which reduces to the classical Rayleigh-Plesset equation [37] when $R_a \to \infty$. Here p_b can be expressed as a function of R according to the equation of state. In this paper we only consider the isothermal expansion or compression of an ideal gas, thus

$$p_b=\left(\frac{R_0}{R}\right)^3\left(p_a+\frac{2\sigma}{R_0}\right), \tag{26}$$

where R_0 is the bubble radius at equilibrium. Supplemented by Eq. (26), Eq. (25) forms an ordinary differential equation for $R(t)$, which can be easily solved by MATHEMATICA. For small amplitude oscillations with $R_a \to \infty$, the natural frequency is given by [37]

$$f = \frac{1}{2\pi}\sqrt{\frac{3p_a + 4\frac{\sigma}{R_0}}{\rho R_0^2}}. \tag{27}$$

We will calculate the bubble oscillation in water using our ALE code in the domain shown in Fig. 3, with $R_a = 10R_0$. The physical parameters are: $\mu = 10^{-3}$ Pa s, $\rho = 10^3$ kg/m^3, σ=0.072 J/m^2, $p_a = 10^5$ Pa. Two equilibrium bubble radii $R_0 = 1$ μm and 10 μm are tested, and the bubble radius is set to $1.75R_0$ at $t = 0$.

At the bubble surface, we use the normal stress condition in Eq. (7). On the outer boundary, the normal stress is fixed at the ambient pressure p_a. As the bubble oscillates, the outer boundary (arc $\widehat{BC}$ in Fig. 3) moves as well. However, the relative variation of R_a is $\frac{\delta R_a}{R_a} \sim \left(\frac{R_0}{R_a}\right)^3 \frac{\delta R}{R_0} \approx 0.001$ for the parameters used here. Thus we have applied the outer boundary condition at a fixed location $r = 10R_0$. This incurs an error in the pressure at $r = R_a$ that is approximately $2\rho\dot{R}^2\left(\frac{R_0}{R_a}\right)^4\frac{\delta R_a}{R_a} \approx 2 \times 10^{-7}\rho\dot{R}^2$, which is negligible. Approximately 50 triangle vertices are deployed along $\widehat{BC}$ and about 25 along $\widehat{DA}$. Because the flow is irrotational and the amplitude of oscillation is not very large, the mesh does not deform much during the whole process. Therefore, remeshing is only performed once or twice within each oscillation cycle. As a result, the total number of elements fluctuates between 2117 and 2173. The time step is taken to be $\Delta t = 0.005t_f$ to ensure temporal accuracy, where $t_f = \frac{R_0}{\sqrt{p_a/\rho}}$ is the time scale for the oscillation. Two thousand steps of time marching take about 1 hour on a 1.0 GHz Pentium III processor.

Figure 4 shows excellent match between finite-element calculations and the exact solution of Eq. (25). Numerical errors, measured against the analytic solution, are given in Table 1 for several grid sizes, which clearly show second-order accuracy in space.

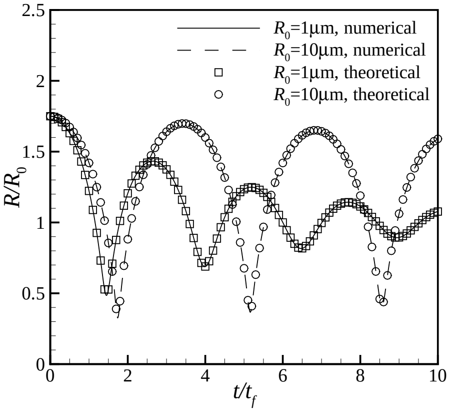

Figure 4: Bubble oscillation in a finite extent of incompressible fluid.

i	Elements along bubble surface (N)	$R_0 = 1\ \mu$m		$R_0 = 10\ \mu$m	
		L_2 error (ϵ)	order (n)	L_2 error (ϵ)	order (n)
1	12	1.18×10^{-3}		7.41×10^{-3}	
2	17	5.75×10^{-4}	2.1	3.71×10^{-3}	2.0
3	25	2.89×10^{-4}	1.8	1.60×10^{-3}	2.2

Table 1: The finite-element solutions for $R(t)$ show second-order accuracy with decreasing grid size. n is defined as $n_i = \log(\epsilon_i/\epsilon_{i-1})/\log(N_{i-1}/N_i)$. For all cases, 2N elements are distributed along the domain outer boundary, and the time step is fixed at $\Delta t = 0.005 t_f$.

3.2 Rise of a bubble in a quiescent liquid

Hnat and Buckmaster studied the different shapes and terminal velocities of bubbles rising in incompressible liquids [38]. Their data have served as benchmark for various numerical codes for interfacial or free surface flows [12, 14, 39, 40]. These are used here to validate the treatment of surface deformation due to external flow. The oscillating bubble of the previous subsection keeps its spherical shape and does not highlight the role of the surface tension.

In particular, we will use the case of Fig. 1(A) in Hnat and Buckmaster [38], with the following fluid parameters: $\rho = 875.5$ kg/m^3, $\mu = 0.118$ Pa s, $\sigma = 3.22 \times 10^{-2}$ J/m^2. The

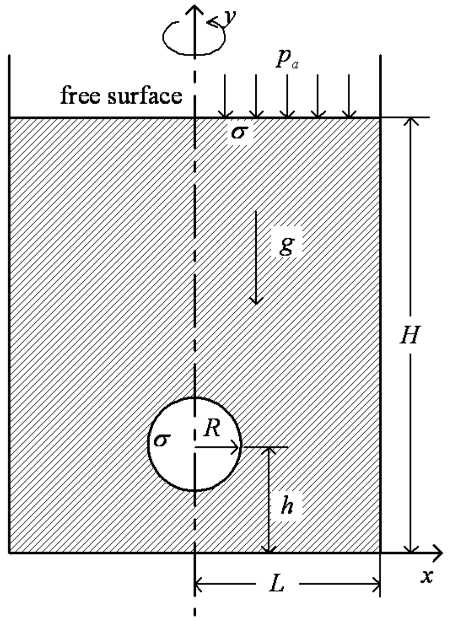

Figure 5: Schematic of the computational domain for the rising bubble.

bubble radius $R = 6.08 \times 10^{-3}$ m, and the gravitational acceleration $g = 9.8$ m/s^2. These form two dimensionless groups: an Eötvos number $Eo = \frac{\rho g (2R)^2}{\sigma} = 39.4$ and a Morton number $M = \frac{g\mu^4}{\rho\sigma^3} = 6.50 \times 10^4$. The experimentally measured terminal rising velocity of the bubble is $U_\infty = 0.215$ m/s. This corresponds to a Reynolds number $Re = \frac{\rho U_\infty R}{\mu} = 9.69$, Weber number $We = \frac{\rho U_\infty^2 R}{\sigma} = 7.64$, and a drag coefficient $C_D = \frac{(4/3\pi R^3)\rho g}{1/2(\pi R^2)\rho U_\infty^2} = 3.44$. Since the experiment was done in a large container with negligible wall effects, we use a very large computational domain with $L = 10R$ and $H = 30R$ as shown in Fig. 5. Because of axisymmetry, only the right half of the meridian plane is calculated. Symmetry conditions are used on the y-axis, while no-slip and slip velocity conditions are imposed at the bottom and right walls, respectively. The upper boundary is treated as a free surface subject to the atmospheric pressure $p_a = 1.01 \times 10^5$ Pa. The bubble is released at $h = 5R$, and the initial pressure is set to be $p_b = p_a + \rho g (H - h) + \frac{2\sigma}{R} = 1.02 \times 10^5$ Pa.

Roughly 100 boundary segments are distributed along the half circle of the bubble surface and 60 along the x-axis, producing around 29,000 finite elements at the beginning. The time step is adjustable during the calculations with a typical value $\Delta t = 4.4 \times 10^{-3} \frac{R}{U_\infty}$. Remeshing is performed about every 40 steps initially because of drop deformation. In

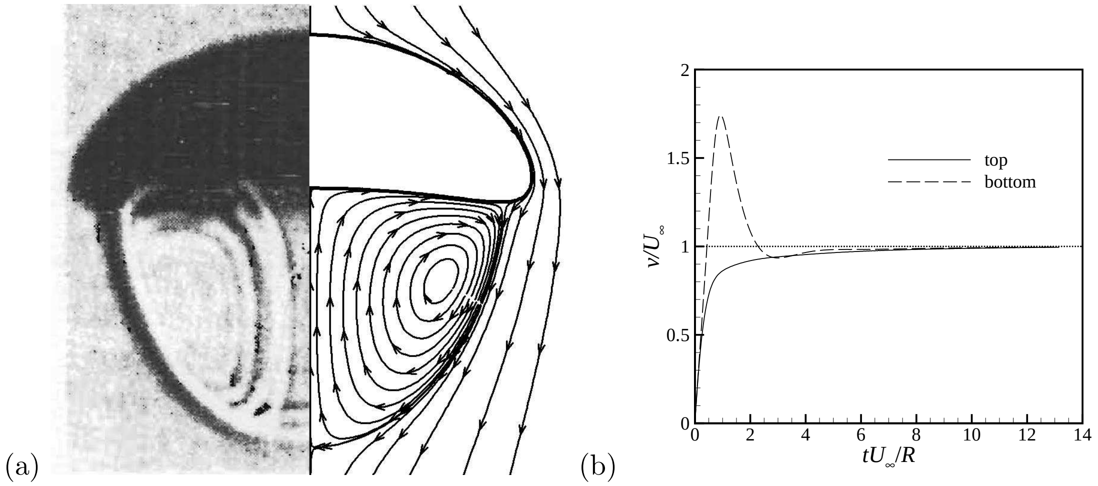

Figure 6: (a) The steady-state bubble shape. The left half is from the experiment of Hnat and Buckmaster [38], while the right half is our simulation. The streamlines are in close agreement as well. (b) The instantaneous velocity at the top and bottom of the bubble, scaled by the experimental terminal velocity U_∞.

the final steady state, much less remeshing is needed if the mesh is allowed to slip on the bubble surface. If the surface nodes do not slip, remeshing occurs once every 20 steps or so. A typical run of 3000 time steps takes less than 15 hours of computation on a 1.0 GHz Pentium III processor.

Comparison with the experiment [38] is shown in Fig. 6. Both the steady-state bubble shape and the flow field in the wake are reproduced accurately by the simulation. At the start of the rise, the bubble flattens. Thus the instantaneous velocity at the bottom of the bubble is significantly larger than at the top. In time, the bubble assumes a steady-state shape of a spherical cap, with a terminal rising velocity that is 99.5% of the experimental U_∞. We also tested a smaller computational domain with $L = 5R$ and $H = 20R$. The wall confinement reduces the terminal velocity slightly to $0.953U_\infty$.

In the simulations, we have treated the gas in the bubble as an ideal gas. Thus, there is a slight expansion of the bubble volume V_b as it rises (Fig. 7). For the parameters used here, the hydrostatic head above the bubble is insignificant as compared to p_a and the increase in V_b is minimal. When we decrease the number of surface segments from 100 to 50, apparent oscillations of the bubble volume become noticeable. This is a numerical artifact due to

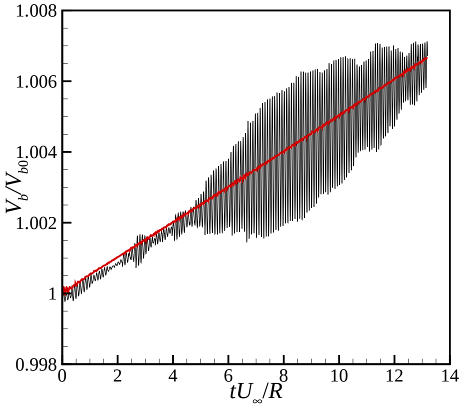

Figure 7: The bubble volume V_b, scaled by the initial volume $V_{b0} = \frac{4}{3}\pi R^3$, increases during the rise. The thick line is for a finer mesh with 100 elements on the bubble surface, while the oscillatory trajectory is for a coarser mesh with 50 surface elements.

remeshing. Each time the number of boundary segments changes, V_b as calculated from the surface nodes changes slightly. Thus remeshing supplies a more or less periodic disturbance to V_b. Interestingly, there is a sort of resonance when the frequency of remeshing is close to that of the natural frequency of the bubble (cf. Eq. 27). With finer grids, the oscillation disappears quickly.

3.3 Single bubble growth

Feng and Bertelo [8] have solved the 1D problem of the diffusion-driven growth of a single spherical bubble in an infinite, initially supersaturated polymer melt. The rheology is represented by the Oldroyd-B model. By solving the same problem in a 2D axisymmetric domain similar to that in Fig. 3, we aim to validate two additional aspects of the code: its handling of diffusion-driven bubble growth and the effect of viscoelasticity. Similarly to Ref. [8], we define the dimensionless groups for bubble growth in an Oldroyd-B melt as: $p_a^* = \frac{p_a R_0^2}{\mu D}$, $Re = \frac{\rho D}{\mu}$, $Ca = \frac{\mu D}{\sigma R_0}$, $\beta = \frac{\mu_s}{\mu}$, $k^* = \frac{k \mu D}{c_0 R_0^2}$, $A^* = RTk$, $De = \frac{\lambda_H D}{R_0^2}$, where R_0 and c_0 are the initial bubble radius and gas concentration. The outer edge of the computational domain is fixed at $R_a = 50R_0$, approximating an infinite sea of melt. On the outer boundary, the normal stress is equal to the ambient pressure p_a, and the gas flux vanishes. The mesh

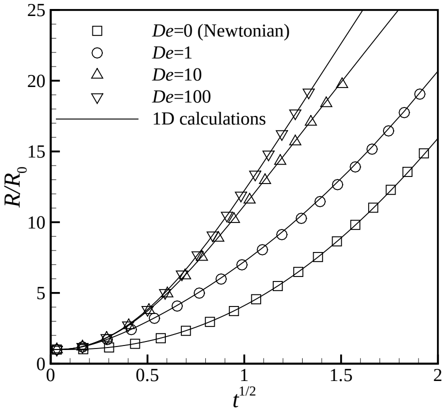

Figure 8: Comparison of bubble growth for different De between ALE calculations (symbols) and previous 1D calculations of Feng and Bertelo [8]. The dimensionless parameters are: $p_a^* = 1$, $Re = 10^{-6}$, $Ca = 2.5$, $\beta = 0.1$, $k^* = 0.01$ and $A^* = 0.11$. The melt is of infinite expanse in the 1D calculations.

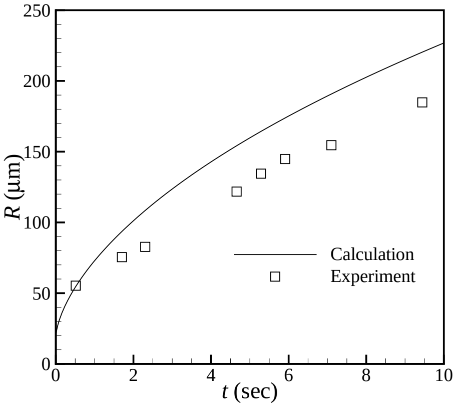

Figure 9: Comparison of bubble growth between ALE calculation with the experimental data of Han and Yoo [41]. The experimental conditions correspond to: $p_a^* = 0.04605$, $Re = 1.21 \times 10^{-10}$, $Ca = 78.57$, $\beta = 0$, $k^* = 4.686$, $A^* = 0.3551$ and $De = 495.0$. The numerical simulation matches all these except for $\beta = 0.1$, and starts with a bubble radius of $R_0 = 20$ μm.

size is approximately $0.063R_0$ on the initial bubble surface and $0.78R_0$ in the bulk region, and there are approximately 19,000 triangular elements overall.

For a wide range of De, Fig. 8 shows excellent agreement between our 2D ALE calculations and the previous 1D calculations [8]. The two solutions only become distinguishable when the bubble grows to a radius $R \sim 20R_0$. That is when the outer boundary starts to exert an influence on the bubble growth in the ALE computation. At $R = 10R_0$, the strain-rate on the bubble surface corresponds to an effective Deborah number $\lambda_H \dot{R}/R = 0.465$, 8.92 and 107 for $De = 1$, 10 and 100. We have also computed bubble growth under conditions corresponding to an experiment on foam extrusion [41]. Figure 9 shows that bubble growth is over-predicted by roughly 20%. The experiment has multiple bubbles growing in an enclosed mold, and competition between neighboring bubbles may have hindered bubble growth. Besides, there is uncertainty in the initial radius of the bubble. In view of these complications, the agreement in Fig. 9 is reasonable.

3.4 Multi-bubble interaction

We consider a two-dimensional foam expanding in ambient pressure p_a. We assume that the foam has large spatial dimensions and consists of monodisperse gas bubbles that form a periodic hexagonal honeycomb pattern (Fig. 10a). These assumptions are reasonable in an average sense for bubbles in the interior of the foam [10]. Due to symmetry of the periodic cell, we only need to consider one twelfth of a single cell as shown in Fig. 10(b). During foam expansion, boundaries BC and DA slide along straight lines, while AB remains vertical and moves to the right.

The boundary conditions on the bubble surface $\widehat{CD}$ are those given by Eqs. (7) and (8). BC and DA are lines of symmetry on which we impose the slip and no-gas-flux conditions:

$$\boldsymbol{v} \cdot \boldsymbol{n} = 0, \tag{28}$$

$$\boldsymbol{n} \cdot (-p\boldsymbol{I} + \boldsymbol{\tau}) \cdot \boldsymbol{t} = 0, \tag{29}$$

$$\boldsymbol{n} \cdot \nabla c = 0, \tag{30}$$

where $\boldsymbol{n}$ and $\boldsymbol{t}$ are the local normal and tangential vectors. AB is also a line of symmetry on which the zero-shear-stress (Eq. 29) and zero-flux (Eq. 30) conditions apply. However, AB moves as a result of foam expansion and Eq. (28) must be replaced by a moving wall condition: $\boldsymbol{n} \cdot \boldsymbol{v} = v_w$, where $v_w(t)$ cannot be prescribed *a priori*. To predict v_w, Everitt

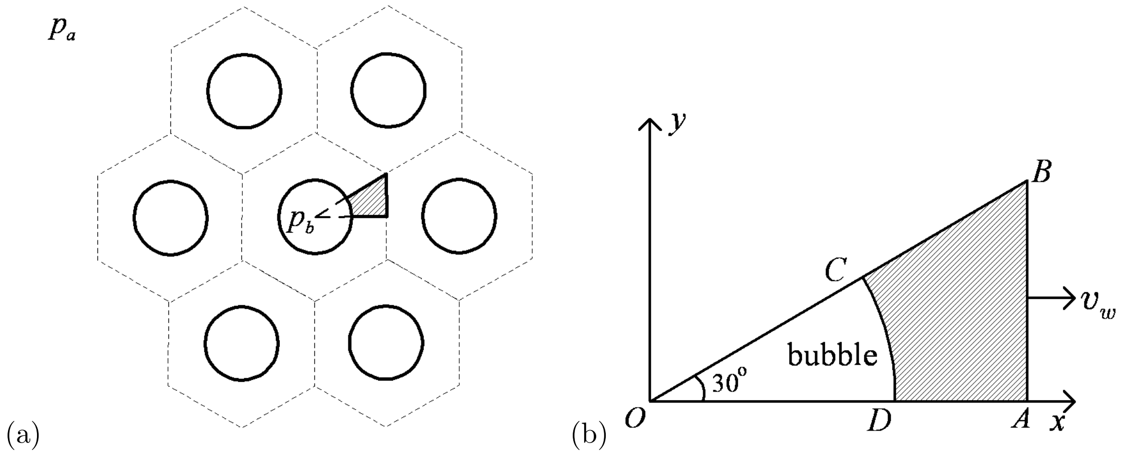

Figure 10: (a) Hexagonal cells in a monodisperse foam. (b) The computational domain is a part of the periodic cell.

et al. [10, 11] introduced an energy equation that relates the work done by the bubble pressure, the ambient pressure and internal stresses to the increasing bubble surface energy. In the following, we derive an alternative condition that is easier to implement in our finite-element algorithm.

When AB moves rightward by an infinitesimal distance δx, the volume of ΔOAB increases by $\delta V = \overline{AB}\delta x$. Then the entire foam expands by $n\delta V$, n being the number of units identical to ΔOAB in the foam. This expansion against the ambient pressure p_a requires an amount of work $n\delta V p_a$. Inside the unit cell ΔOAB, the only work output is by the normal stress on AB. Adding such output from all n cells and equating the sum to the total work against p_a, we obtain:

$$\int_{AB} \boldsymbol{n}\cdot(-p\boldsymbol{I}+\boldsymbol{\tau})\,dS = -p_a\overline{AB}. \tag{31}$$

Note first that this condition represents the force balance governing foam expansion, an average normal stress in the foam being equated to the ambient pressure. Second, this condition concerns only the work of expanding the foam, and is not an energy balance. However, if coupled with the momentum equation, Eq. (31) should be consistent with the energy equation of Everitt *et al.* [10, 11]. Finally, this extra boundary condition can be easily incorporated into our Galerkin weak form, and exactly compensates for the extra

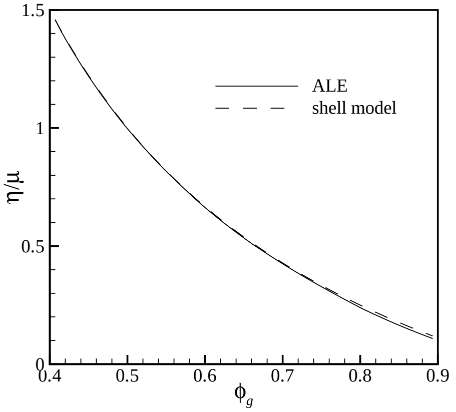

Figure 11: Expansion viscosity of a 2D foam. The solid curve is computed from a 2D ALE simulation using Eq. (32), while the dashed one represents Eq. (33).

unknown v_w. The moving wall condition amounts to $-p_a\overline{AB}\tilde{v}_w$ in the surface integral in Eq. (15).

As a validation of the periodic-cell assumption and the boundary condition in Eq. (31), we first compute the expansion viscosity of a Newtonian foam. The expansion viscosity is defined as:

$$\eta = \frac{(p_b - \frac{\sigma}{R} - p_a)}{\frac{\dot{V}_f}{V_f}}, \tag{32}$$

where V_f is the foam volume (the sum of bubble volume and melt volume) and R is the equivalent bubble radius. Using a 1D shell model (cf. Fig. 3) to represent the bubble and its surrounding melt, Kraynik *et al.* [6] calculated η for a planar foam:

$$\eta = \mu\frac{1-\phi_g}{\phi_g}, \tag{33}$$

where $\phi_g = \frac{R^2}{R_a^2}$ is the instantaneous gas volume fraction. To simulate the same process in our 2D domain (Fig. 10), we turn off gas diffusion and consider the expansion of bubbles having a high initial bubble pressure. Our initial conditions are $\overline{OA} = 1.5R_0$ and $p_b = 21p_a$, and the ambient pressure is $p_a = \sigma R_0$. We record the temporal evolutions of p_b, R and the volume ΔOAB, and use Eq. (32) to evaluate the foam expansion viscosity. Figure 11 shows close agreement of our ALE computation with Eq. (33). Discrepancy becomes apparent after

$\phi_g \approx 0.7$, when the bubble starts to deviate from the circular shape in our simulations. Thus we conclude that our geometric setup and boundary conditions work well. We have also computed η when the foam expansion is driven by gas diffusion instead of an initially elevated bubble pressure. Similar agreement with Eq. (33) is observed.

In simulating diffusion-driven foam expansion, we use p_a, R_0, k and μ to non-dimensionalize all the variables, e.g., scaling time by $\frac{\mu}{p_a}$. The following parameters are used: $A^* = RTk = 1$, $D^* = \frac{D\mu}{p_a R_0^2} = 1$, $\sigma^* = \frac{\sigma}{p_a R_0} = 1$, and the melt is inertialess. Initially, $L = \overline{OA} = 1.2R_0$, $c_0^* = \frac{c_0}{kp_a} = 20$, and $p_b^* = \frac{p_b}{p_a} = 2$. Thus the system is in mechanical equilibrium but not thermodynamic equilibrium; gas diffusion from the supersaturated melt will drive the bubble growth. With a viscoelastic melt, two extra parameters are needed: $De = \frac{\lambda_H p_a}{\mu}$ and $\beta = \frac{\mu_s}{\mu}$. Initially, the polymer molecules are coiled and the polymer stress is nil. In the following we drop the superscript * for dimensionless variables where such omission does not cause confusion. Mesh size is about 0.014 in the melt, and the total number of triangular elements is roughly 2000. As an indication of the accuracy of the simulations, melt volume is conserved to within 3×10^{-5} during foam expansion, while the total mass of gas is conserved to within 2%. Almost all the mass loss for gas occurs in the first several time steps; the initial sharp boundary layer of c at the bubble surface is difficult to resolve accurately. This mass loss can be reduced to within 4×10^{-4} if we use $c_0^* = p_b^* = 8$ as the initial condition, in which case the system is in thermodynamic equilibrium and has no boundary layer of c at $t = 0$.

Foam expansion is illustrated in Fig. 12 by the increase of the domain size $L = \overline{OA}$ and the decrease of the thinnest film thickness $h_{film} = \overline{DA}$ (cf. Fig. 10b). For Newtonian and viscoelastic melts alike, the results clearly exhibit two stages of foam growth. The first is diffusion-driven rapid expansion ($0 < t \lesssim 0.2$). The rapid growth in bubble size is accompanied by an equally rapid decline in the gas concentration in the melt, depicted by the contour plots in Fig. 13(a). In this stage, the pressure is lower at the film center (Point A in Fig. 10b) than in the Plateau border (Point B). This is because the melt experiences more severe squeezing at the film center and thus develops greater viscous or viscoelastic normal stress. The hydrodynamic pressure is consequently lower so as to maintain force balance around the bubble surface. The second stage features capillarity-driven film drainage ($t \gtrsim 0.2$). Having exhausted most of the dissolved gas in the melt, the bubble gains little mass or volume in this stage, and the foam essentially stops expanding

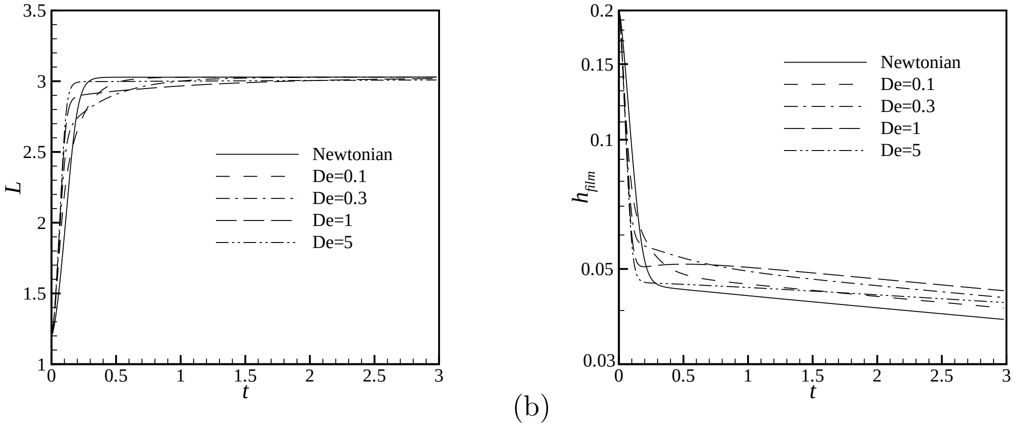

(a) (b)

Figure 12: (a) Temporal growth of the foam size indicated by $L = \overline{OA}$. (b) Evolution of the film thickness $h_{film} = \overline{DA}$. For all non-Newtonian melts $\beta = 0.5$.

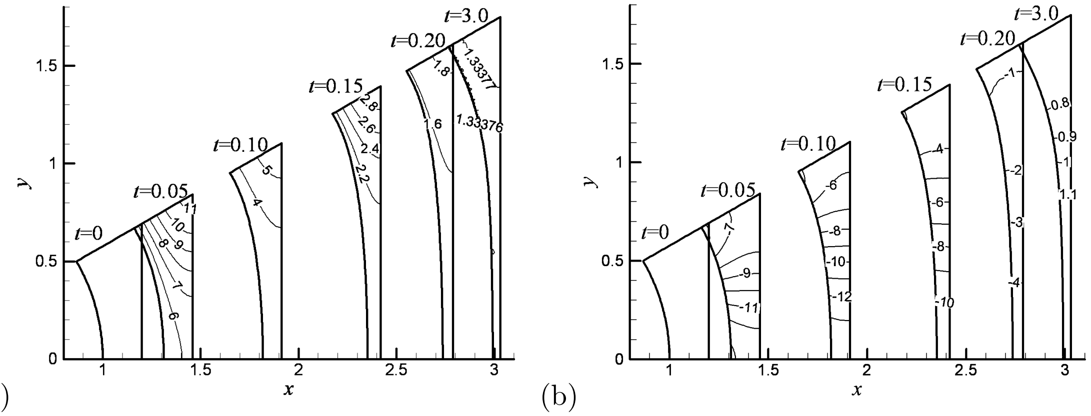

(a) (b)

Figure 13: (a) Distribution of the concentration of dissolved gas during foaming. The initial concentration is $c_0 = 20$ at $t = 0$. (b) Pressure distribution within the melt. The melt is Newtonian and the process corresponds to the Newtonian curves in Fig. 12.

(Fig. 12a). Note in Fig. 13(a) the nearly uniform c through out the melt at $t = 3.0$. As the bubble surface deviates from a circular shape, however, the curvature difference creates a capillary pressure that is lower in the Plateau border than at the center of the film, contrary to the previous stage (Fig. 13b). This drives the film drainage [42] and the continual, albeit slow, decrease of the film thickness h_{film} (Fig. 12b).

Viscoelastic effects differ markedly between the two stages. In the first stage, the foam

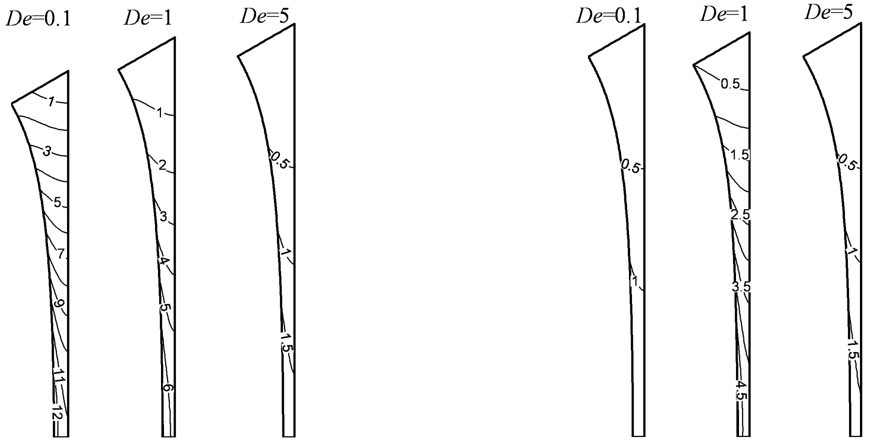

(a) $t = 0.2$ (b) $t = 0.5$

Figure 14: Contours of the tensile stress τ_{pyy} in the viscoelastic film. (a) Buildup of τ_{pyy} toward the end of the rapid expansion stage, and (b) its subsequent relaxation in the film drainage stage.

expands more rapidly as the polymer relaxation time λ_H (or De) increases. This is because the polymer stress develops more slowly at larger De, and the melt initially appears to be less viscous upon start of deformation. A similar scenario has been identified for viscoelastic effects on drop coalescence [43]. For much of the second stage, on the other hand, the melt film is thicker in viscoelastic melts than in the Newtonian melt. This may be rationalized by the fact that polymer stresses developed during foam expansion now resist further growth of the foam and thinning of the polymer film. The two-stage scenario has been previously reported by Everitt *et al.* [10] for viscoelastic melts in the high-De limit. In our simulations, the second stage comes about for all De, and even for Newtonian fluids.

Viscoelasticity in stage two exhibits two additional features that are somewhat unexpected. First, the effect of De is no longer monotonic; the thickest film and the slowest foam expansion are observed for an intermediate $De = 1$. This is the result of two competing factors: the accumulation of polymer stress during the foam expansion stage and its subsequent relaxation in the film drainage stage. As illustrated by Fig. 14, the polymer tensile stress τ_{pyy} rises quickly to large values for a low $De = 0.1$, only to relax shortly into the film drainage stage. For a large $De = 5$, the polymer stress attained during foam expansion is so small that its longevity amounts to little. It is at an intermediate De that the viscoelasticity resists foam expansion most effectively, through a polymer stress that is both relatively large and long lasting. The second surprising feature is the undershoot in the film thickness h_{film} for $De = 1$ in Fig. 12(b). This is due to the polymer stress τ_{pyy} that has arisen, along with τ_{pxx}, from the roughly planar elongational flow in the film. Countering capillary drainage, τ_{pyy} tends to pull the fluid from the Plateau border (Point B in Fig. 10b) toward the film center (Point A). At its peak, this stress is large enough to reverse the film thinning temporarily, and then declines as the polymer relaxes in the second stage. Hence the undershoot in h_{film}. Everitt *et al.* [10] observed a similar undershoot and explained it similarly by polymer recoil. When we increase the polymer stress relative to the viscous stress in the constitutive equation by decreasing $\beta = \mu_s/\mu$, the undershoot becomes more prominent, in agreement with Everitt *et al.* [10].

To summarize the viscoelastic effects on bubble growth, strain-hardening, namely the sharp growth of polymer stresses in extensional flows, is the most important rheological property in foaming. That these stresses tend to hinder bubble growth is well known. In fact, high-molecular-weight additives are frequently used to increase the "melt strength", which will prevent excessive growth and burst of bubbles and produce more uniform bubble sizes and better foam expansion [44]. Previous calculations of single bubble growth are able to predict the initial fast growth in viscoelastic melts [8], but not the subsequent film thinning as governed by the interaction between neighboring bubbles.

We have also explored bubble interactions in a non-periodic geometry, and Fig. 15 illustrates the growth of a cluster of bubbles in a Newtonian melt. Initially, bubbles of the same radius R_0 are arranged in a hexagonal pattern, the distance between neighboring bubbles being $2.4R_0$. The computational domain is a circle of radius $30R_0$ centered around the bubbles. On the outer boundary, the normal stress is set to the ambient pressure and the gas flux vanishes. The initial gas concentration is $c_0^* = 8$, the initial bubble pressure is $p_b^* = 8$, and all other parameters are the same as the Newtonian simulation in Fig. 12. Thus the system is in thermodynamic equilibrium but not mechanical equilibrium. As the bubbles grow, the whole cluster expands. Depending on the competition for dissolved gas between neighboring bubbles, four bubble sizes emerge. The six bubbles at the corners of the outer hexagon grow the fastest, because they have access to the gas-rich melt on the

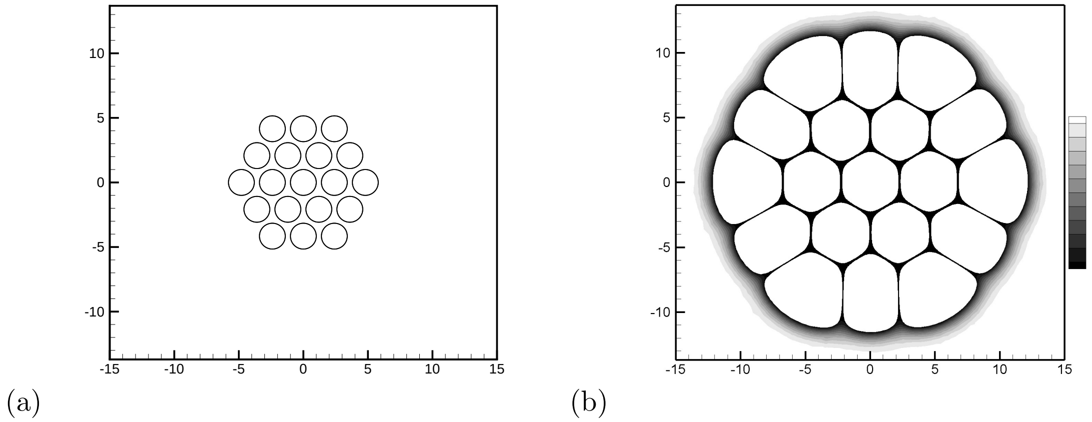

Figure 15: Growth of a cluster of bubbles in a Newtonian melt. (a) $t = 0$; (b) $t = 0.7974$. The grey-scale contours indicate the gas concentration c^*. Initially $c_0^* = 8$.

outside with the least competition from other bubbles. These are followed by the non-corner bubbles on the outer layer and in turn by the inner hexagon. The central bubble grows the slowest. As the bubbles press against one another, thin films form between them and the inner bubbles assume approximately hexagonal shapes (Fig. 15b). This may be considered the prototype for the periodic cell of Fig. 10. Furthermore, Fig. 15 shows the competition between neighboring bubbles to be one cause for polydispersity in real foams, besides continual nucleation and age differences. Note that Fig. 15(b) is far from a "final equilibrium" and the bubbles will continue to grow until all the dissolved gas is consumed. Quantitatively, the central bubble grows at a lower rate than in the periodic geometry of Fig. 10 under comparable conditions. This is because in the non-periodic setup, each bubble displaces more polymer melt on average than in the periodic setup.

3.5 Film drainage between a bubble and a free surface

Given that higher melt strength suppresses bubble growth, it seems counterintuitive that it also produces greater foam expansion [44]. The explanation lies in the fact that higher polymer stresses prevent burst of bubbles at the surface of the foam and loss of blowing agent into the atmosphere. This has motivated our investigation of the interaction between a bubble and a free surface. At the surface, however, bubble-bubble interactions can no

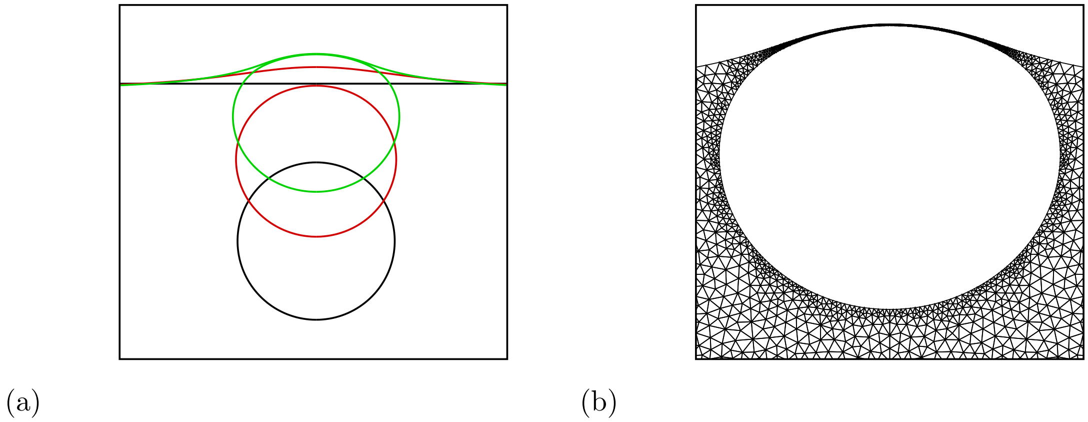

Figure 16: A bubble pressing against a free surface in a Newtonian melt. (a) Snapshots of the interfacial morphology at $t = 0$, 9.85, and 20.45. (b) Computational mesh around the bubble at $t = 20.45$.

longer be represented by the periodic cells of Fig. 10. Without including a large number of bubbles, it is difficult to simulate the squeezing among bubbles that thrusts the outmost ones against the free surface. As an expedient, we have used a buoyancy force to drive the bubble upward toward an initially horizontal free surface. Since gas diffusion is insignificant in the film drainage stage, we have neglected it completely. In real systems, surfactants may affect film drainage by immobilizing the surfaces [45]. This will not be considered here. We concentrate on the influence of rheology on film drainage between the bubble and the free surface.

We use the axisymmetric computational domain of Fig. 5. All parameters and variables are made dimensionless by the initial bubble radius R, liquid density ρ and viscosity μ. The geometric parameters are $L = 4$, $H = 5$ and $h = 3$, and the flow parameters are such that the Eötvos number $Eo = \frac{\rho g (2R)^2}{\sigma} = 2$ and the Ohnesorge number $Oh = \frac{\mu}{\sqrt{\rho\sigma(2R)}} = \frac{\sqrt{2}}{2}$. For viscoelastic fluids, we use $\beta = \frac{\mu_s}{\mu} = 0.5$ and three relaxation times are calculated: $\lambda_H = 1$, 2 and 10. Ambient pressure is set to $p_a = 300$ such that the bubble volume increases less than 1% during its rise. Initially, 75 and 50 mesh nodes are distributed along the bubble surface and radial direction, respectively. This corresponds to roughly 4000 finite elements. Numerical experiments show these to be sufficient for convergence with grid size.

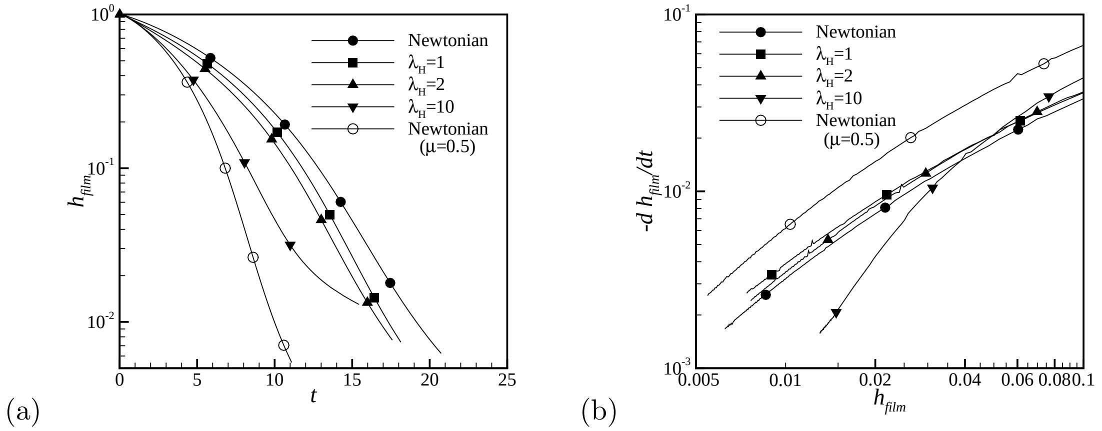

Figure 17: Thinning of the film between the bubble and the free surface. (a) The film thickness h_{film} as a function of time. (b) The thinning rate as a function of h_{film}. Viscoelastic melts with three relaxation times are compared with a Newtonian melt of the same total viscosity μ. A Newtonian melt with the solvent viscosity μ_s is also shown.

In a Newtonian melt, the evolution of the bubble and free surfaces is shown in Fig. 16(a). At $t = 9.85$, a dome is formed on the free surface which provides a downward surface force to counter the buoyancy of the bubble. At $t = 20.45$, the film has drained to a very small thickness $h_{film} = 6.75 \times 10^{-3}$, less than 1% of the bubble radius. Resolution of such films poses a numerical challenge, which is handled in our case by adaptively refining the mesh in the film as shown in Fig. 16(b). Even the thinnest part of the film contains two or three layers of interior nodes. However, with the decreasing mesh size comes an increasingly severe constraint on the time step even for our fully implicit method. We have to use $\Delta t = 0.001$ to march beyond $t = 20$. Larger Δt tends to cause undulations on the surfaces and destabilize the thin film. For viscoelastic systems, the constraint on Δt is even more restrictive.

For a viscoelastic melt, the general features of film thinning are the same as for a Newtonian melt, but the thinning rate depends on the Deborah number, as depicted in Fig. 17. Approximating the flow in the film by the startup of biaxial extension at a constant rate $\dot{\epsilon}_0 < 0$, the transient elongational viscosity for an Oldroyd-B fluid is [31]

$$\bar{\eta}^+ = 3\mu\left[\beta + \frac{1-\beta}{(1-De)(1+2De)}\right] - \frac{\mu(1-\beta)}{1-De}e^{-\frac{t}{\lambda_H}(1-De)} - \frac{2\mu(1-\beta)}{1+2De}e^{-\frac{t}{\lambda_H}(1+2De)}, \quad (34)$$

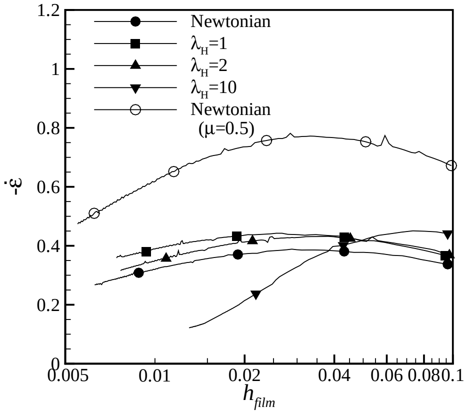

Figure 18: Strain rate $\dot{\epsilon}$ for the biaxial extension in the film as a function of the film thickness.

where $De = -\dot{\epsilon}_0 \lambda_H$ is the local Deborah number. It is easy to see that $\bar{\eta}^+ = 3\beta\mu$ at $t = 0$, which is the purely viscous contribution of the solvent. Because the polymer stress needs time to build up, this initially lower $\bar{\eta}^+$ causes the viscoelastic films to thin faster at the early stage than the Newtonian film with the same total viscosity μ. However, due to the effect of solvent viscosity, all the viscoelastic curves are bounded by the Newtonian curve with $\mu = 0.5$.

To understand the long-time behavior of the film, we note that the steady-state elongational viscosity

$$\bar{\eta} = \lim_{t\to\infty} \bar{\eta}^+(t) = 3\mu \left[\beta + \frac{1-\beta}{(1-De)(1+2De)}\right] \tag{35}$$

is non-monotonic in De. For $\beta = 0.5$, we have

$$\begin{cases} \frac{17}{6}\mu \le \bar{\eta} \le 3\mu & \text{for } De \in [0, 0.5] \\ 3\mu < \bar{\eta} < \infty & \text{for } De \in (0.5, 1) \\ \bar{\eta} \to \infty & \text{for } De \in [1, \infty) \end{cases} . \tag{36}$$

If $De < 0.5$, $\bar{\eta}$ of the viscoelasticity fluid is always smaller than its Newtonian counterpart 3μ. For $De > 0.5$, $\bar{\eta}$ will eventually exceed the Newtonian value, and indeed will grow without bound if $De \ge 1$.

To ascertain the polymer stress in the film, we define an effective strain-rate $\dot{\epsilon} = \frac{1}{h_{film}}\frac{dh_{film}}{dt}$, whose variations with the film thickness are depicted in Fig. 18. For $0.01 <$

$h_{film} < 0.1$, $-\dot{\epsilon} = 0.40 \pm 0.04$, 0.38 ± 0.06 and 0.28 ± 0.16 for $\lambda_H = 1$, 2 and 10, respectively. The corresponding local Deborah numbers fall exactly in the three ranges of Eq. (36). Bearing this in mind, it is quite straightforward to explain the long-time tendency of the curves in Fig. 17. For $\lambda_H = 1$, the film drains faster than its Newtonian counterpart at all times because the viscoelastic elongational viscosity is always below 3μ. In fact, the difference in thinning rates between the two tends to grow in time. The $\lambda_H = 2$ curve in Fig. 17(b), on the other hand, approaches the Newtonian curve in time because $De > 0.5$ and $\bar{\eta}^+$ will eventually exceed 3μ. At $\lambda_H = 10$, the thinning rate drops dramatically toward the end as $\bar{\eta}^+$ grows rapidly for $De > 1$. Although we did not carry on the calculation further, the trend in Fig. 17(a) suggests that the polymer film for $\lambda_H = 10$ will eventually become thicker than the Newtonian one. Another noteworthy feature of Fig. 18 is that the Newtonian strain-rate for $\mu = 1$ remains approximately half of that for $\mu = 0.5$. This is because the film drainage is a quasi-static Stokes flow with a time scale proportional to the liquid viscosity.

The film drainage here is driven by a constant buoyancy force, and the process is somewhat simpler than in the last subsection, where the film drainage is induced by capillary forces after earlier foam expansion has produced a curvature gradient along the bubble surface. Nevertheless, the polymer rheology is manifested through the same fundamental mechanism of strain-hardening. This causes the steep decline in thinning rate for the longest λ_H in Fig. 17(b). In the same vein, the lowest film thinning rate in the second stage occurs for the highest De in Fig. 12(b).

In reality, the film bursts once it gets to a critical thickness where short-range molecular forces such as van der Waals attraction become dominant. Absent such non-hydrodynamic effects, the film thickness h_{film} will not decrease to zero in finite time, as can be readily shown by a lubrication analysis. Numerically, our mesh size continues to decrease with h_{film}, and the simulations eventually grinds to a halt. The simulations in the last subsection (cf. Fig. 12b) has the same fate. To properly simulate film burst, the short range forces have to be accounted for [43].

4 Conclusion

In this work, we have developed an arbitrary Lagrangian-Eulerian scheme for tracking bubble surfaces during foaming, and validated the algorithm and finite-element code by benchmark problems. A moving mesh tracks the interfaces accurately, with adaptive refinement and coarsening based on surface curvature and proximity between surfaces. Fully implicit time-stepping enhances numerical stability and ensures smoothness of the surface curvature. Iterative schemes such as preconditioned GMRES and BICGSTAB are used to solve the linear system. With gas diffusion included, the scheme proves to be accurate and efficient for simulating polymer foaming. But the algorithm and numerical package apply generally to free-boundary problems of viscoelastic fluids.

We have simulated diffusion-driven expansion of a 2D foam as well as the thinning of a film between a bubble and a free surface. Results show strain-hardening to be the most important rheological property for polymer foaming, which mostly involves biaxial extension of the melt. A significant insight from the simulations is that the elongational viscosity of the polymer melt helps stabilize the foam structure by suppressing bubble-bubble coalescence and bubble burst at the foam surface. The two simulations are consistent with prior experimental observations that (a) increasing the melt strength results in smaller but more uniform bubble sizes, and (b) increasing the melt strength produces greater foam expansion in the end as the polymer stresses prevent burst and collapse of bubbles on the surface of the foam.

We end by pointing out the limitations of the current work. Although the Oldroyd-B model gives the correct trend in strain-hardening, it does not quantitatively capture the rheology of typical polymer melts. More elaborate constitutive equations are required if the results are to be used to guide process design. Second, real foams feature a bubble-size distribution, with spatially and temporally random nucleation and growth. Direct simulation of such a foam requires the inclusion of a large number of bubbles, and the computational cost is still prohibitive at present. As noted in the text, this also hampers a realistic depiction of bubbles thrust against the foam surface. Finally, we have neglected non-hydrodynamic effects that are important to the actual foaming process. For instance, temperature variations in space and time, along with solidification, are crucial to foam extrusion. Plasticization of the melt by the dissolved gas may also have an important part [26]. To simulate interfacial rupture as occurs in bubble burst or coalescence, short-range molecular forces have to be incorporated [43]. Therefore, much research remains to be done in simulating polymer foaming.

Acknowledgment: This research was supported in part by Arkema Inc. J.J.F. was also supported by the NSERC, the Canada Research Chair program and the Canada Foundation for Innovation. We thank Andrew M. Kraynik for suggesting the comparison in Figure 11.

References

[1] D. Klempner, K. C. Frisch, editors, Handbook of Polymeric Foams and Foam Technology, Hanser Publishers, New York, 1991.

[2] H. X. Peng, Z. Fan, J. R. G. Evans, J. J. C. Busfield, Microstructure of ceramic foams, J. Eur. Ceramic Soc. 20(7) (2000) 807–813.

[3] T. Beechem, K. Lafdi, A. Elgafy, Bubble growth mechanism in carbon foams, Carbon 43 (2005) 1055–1064.

[4] I. Sevostianov, J. Kováčik, F. Simančík, Elastic and electric properties of closed-cell aluminum foams: Cross-property connection, Mater. Sci. Eng. A 420 (2006) 87–99.

[5] A. D. Gopal, D. J. Durian, Shear-induced ‘melting’ of an aqueous foam, J. Colloid Interface Sci. 213 (1999) 169–178.

[6] A. M. Kraynik, D. A. Reinelt, M. Loewenberg, Foam microrheology, In D. Weaire, J. Banhart, editors, Foams and Films, Proceedings of the International Workshop of Foams and Films, pages 97–104, Leuven, Belgium, March 1999.

[7] A. M. Kraynik, D. A. Reinelt, F. van Swol, Structure of random monodisperse foam, Phys. Rev. E 67 (2003) 031403.

[8] J. J. Feng, C. A. Bertelo, Prediction of bubble growth and size distribution in polymer foaming based on a new heterogeneous nucleation model, J. Rheol. 48(2) (2004) 439–462.

[9] T. R. Tuladhar, M. R. Mackley, Experimental observations and modelling relating to foaming and bubble growth frompentane loaded polystyrene melts, Chem. Eng. Sci. 59 (2004) 5997–6014.

[10] S. L. Everitt, O. G. Harlen, H. J. Wilson, Bubble growth in a two-dimensional viscoelastic foam, J. Non-Newtonian Fluid Mech. 137 (2006) 46–59.

[11] S. L. Everitt, O. G. Harlen, H. J. Wilson, Competition and interaction of polydisperse bubbles in polymer foams, J. Non-Newtonian Fluid Mech. 137 (2006) 60–71.

[12] D. Gueyffier, J. Li, A. Nadim, R. Scardovelli, S. Zaleski, Volume-of-fluid interface tracking with smoothed surface stress methods for three-dimensional flows, J. Comput. Phys. 152 (1999) 423–456.

[13] M. van Sint Annaland, N. G. Deen, J. A. M. Kuipers, Numerical simulation of gas bubbles behaviour using a three-dimensional volume of fluid method, Chem. Eng. Sci. 60 (2005) 2999–3011.

[14] M. Sussman, P. Smereka, Axisymmetric free boundary problems, J. Fluid Mech. 341 (1997) 269–294.

[15] G. Tryggvason, B. Bunner, A. Esmaeeli, D. Juric, N. Al-Rawahi, W. Tauber, J.Han, S. Nas, Y.-J. Jan, A front-tracking method for the computations of multiphase flow, J. Comput. Phys. 169 (2001) 708–759.

[16] T. Ye, Wei Shyy, J. N. Chung, A fixed-grid, sharp-interface method for bubble dynamics and phase change, J. Comput. Phys. 174 (2001) 781–815.

[17] E. D. Wilkes, S. D. Phillips, O. A. Basaran, Computational and experimental analysis of dynamics of drop formation, Phys. Fluids 11(12) (1999) 3577–3598.

[18] X. Frank, H. Z. Li, Complex flow around a bubble rising in a non-Newtonian fluid, Phys. Rev. E 71 (2005) 036309.

[19] H. W. Zheng, C. Shu, Y. T. Chew, A lattice Boltzmann model for multiphase flows with large density ratio, J. Comput. Phys. 218 (2006) 353–371.

[20] P. Yue, C. Zhou, J. J. Feng, C. F. Ollivier-Gooch, H. H. Hu, Phase-field simulations of interfacial dynamics in viscoelastic fluids using finite elements with adaptive meshing, J. Comput. Phys. 219 (2006) 47–67.

[21] R. Gendron, L. E. Daigneault, L. M. Caron, Rheological behavior of mixtures of polystyrene with HCFC 142b and HFC 134a, J. Cell. Plastic. 35 (1999) 221–246.

[22] D. C. Venerus, N. Yala, B. Bernstein, Analysis of diffusion-induced bubble growth in viscoelastic liquids, J. Non-Newtonian Fluid Mech. 75 (1998) 55–75.

[23] S. L. Everitt, O. G. Harlen, H. J. Wilson, D. J. Read, Bubble dynamics in viscoelastic fluids with application to reacting and non-reacting polymer foams, J. Non-Newtonian Fluid Mech. 114 (2003) 83–107.

[24] S. N. Leung, C. B. Park, D. Xu, H. Li, R. G. Fenton, Computer simulation of bubble-growth phenomena in foaming, Ind. Eng. Chem. Res. 45 (2006) 7823–7831.

[25] N. S. Ramesh, N. Malwitz, A non-isothermal model to study the influence of blowing agent concentration on polymer viscosity and gas diffusivity in thermoplastic foam extrusion, J. Cell. Plastic. 35 (1999) 199–209.

[26] X. Chen, J. J. Feng, C. A. Bertelo, Plasticization effects on bubble growth during polymer foaming, Polym. Eng. Sci. 46(1) (2006) 97–107.

[27] S. Popinet, S. Zaleski, Bubble collapse near a solid boundary: a numerical study of the influence of viscosity, J. Fluid Mech. 464 (2002) 137–163.

[28] A. Caboussat, M. Picasso, J. Rappaz, Numerical simulation of free surface incompressible liquid flows surrounded by compressible gas, J. Comput. Phys. 203 (2005) 626–649.

[29] A. Caboussat, A numerical method for the simulation of free surface flows with surface tension, Computers & Fluids 35 (2006) 1205–1216.

[30] H. H. Hu, N. A. Patankar, M. Y. Zhu, Direct numerical simulations of fluid-solid systems using the arbitrary lagrangian-eulerian technique, J. Comput. Phys. 169 (2001) 427–462.

[31] R. B. Bird, R. C. Armstrong, O. Hassager, Dynamics of Polymeric Liquids, Vol. 1. Fluid Mechanics, Wiley, New York, 1987.

[32] H. H. Hu, Direct simulation of flows of solid-liquid mixtures, Int. J. Multiphase Flow 22(2) (1996) 335–352.

[33] F. Hecht, E. Saltel, Emc^2 un logiciel d'edition de maillages et de contours bidimensionnels, Technical Report 0118, INRIA, 1990.

[34] P. J. Frey, P.-L. George, Mesh Generation, application to finite elements, Hermes Science Publishing, Oxford & Paris, 2000.

[35] H. S. Udaykumar, R. Mittal, Wei Shyy, Computation of solid-liquid phase fronts in the sharp interface limit on fixed grids, J. comput. Phys. 153 (1999) 535–574.

[36] M. Dai, H. Wang, J. B. Perot, D. P. Schmidt, Direct interface tracking of droplet deformation, Atomization Spray 12 (2002) 721–735.

[37] M. S. Plesset, A. Prosperetti, Bubble dynamics and cavitation, Ann. Rev. Fluid Mech. 9 (1977) 145–185.

[38] J. G. Hnat, J. D. Buckmaster, Spherical cap bubbles and skirt formation, Phys. Fluids 19(2) (1976) 182–194.

[39] G. Ryskin, L. G. Leal, Numerical solution of free-boundary problems in fluid mechanics. Part 2. Buoyancy-driven motion of a gas bubble through a quiescent liquid, J. Fluid Mech. 148 (1984) 19–35.

[40] M. Ohta, T. Imura, Y. Yoshida, M. Sussman, A computational study of the effect of initial bubble conditions on the motion of a gas bubble rising in viscous liquids, Int. J. Multiph. Flow 31 (2005) 223–237.

[41] C. D. Han, H. J. Yoo, Studies on structural foam processing. part iv: Bubble growth during molding filling, Polym. Eng. Sci. 21(9) (1981) 518–533.

[42] A. Bhakta, E. Ruckenstein, Decay of standing foams: drainage, coalescence and collapse, Adv. Colloid Interface Sci. 70 (1997) 1–124.

[43] P. Yue, J. J. Feng, C. Liu, J. Shen, Diffuse-interface simulations of drop coalescence and retraction in viscoelastic fluids, J. Non-Newtonian Fluid Mech. 129 (2005) 163–176.

[44] J. Sandler, F. Wöllecke, V. Altstädt, E. Wettstein, D. Rakutt, Principal correlation of PVC melt elongational properties with foam cell morphology, Cellular Polym. 19 (2000) 371–388.

[45] K. Malysa, M. Krasowska, M. Krzan, Influence of surface active substances on bubble motion and collision with various interfaces, Adv. Colloid Interface Sci. 114-115 (2005) 205–225.